phys. stat. sol. (a) **104**, 743 (1987)

Subject classification: 61.80 and 73.40; 79.20; S5.11

Mechanical, Aerospace, and Nuclear Engineering Department, University of California, Los Angeles[1])

Monte Carlo Simulation of Coupled Ion–Electron Transport in Semiconductors[2])

By

R. C. MARTIN and N. M. GHONIEM

The Monte Carlo ion-transport code TRIPOS is extended to a new version, TRIPOS-E, for modeling secondary-electron generation and transport along ion tracks. Energy deposition and radial electron-hole (e–h) pair profiles in silicon are evaluated for several energetic heavy ions. These profiles reflect a Gaussian-like central core which decreases exponentially at increasing radial distance. Analytical expressions for radial charge-density profiles at several depths of penetration are obtained. The excess charge density remains above background dopant concentrations beyond 0.25 μm radius from the ion path. This detailed evaluation of track structure should enhance modeling of charge collection from ion tracks in semiconductor devices.

Der Monte-Carlo-Ion-Transport-Code TRIPOS wird zu einer neuen Fassung, TRIPOS-E, für die Modellierung von Erzeugung und Transport von Sekundärelektronen entlang Ionenspuren, erweitert. Für mehrere energetisch schwere Ionen in Silizium werden die Energieablagerung und die radialen Elektron–Loch-Paar-Profile abgeschätzt. Diese Profile widerspiegeln einen gaußartigen zentralen Kern, der mit zunehmender radialer Entfernung exponentiell abfällt. Für mehrere Profile der radialen Ladungsdichten werden für verschiedene Eindringtiefen analytische Ausdrücke gefunden. Für Radien größer als 0,25 μm hat die Überschuß-Ladungsdichte einen höheren Wert als den „Doptierungs"-Hintergrundwert. Die ausführliche Bewertung der Spurenstruktur kann für die Modellierung der Ladungssammlung von Ionenspuren in Halbleitern genutzt werden.

1. Introduction

During the past several years, interest in the effects of radiation on semiconductors has grown significantly because of the increase in space and defense applications. Transient charge collection from cosmic ion tracks passing through integrated circuit junctions is known to produce logic upset and memory change. These events are referred to single event upsets (SEUs), and are of two types: (i) soft errors, which involve inversion of the logic state without permanent damage to the circuitry; (ii) latch-up (or hard) errors which permanently fix the logic state of the junction.

The free electrons produced along an ion track within an integrated circuit either recombine with the holes or are collected at the p–n junction as a transient current spike. The high density of these charge carriers significantly alters equilibrium charge carrier distributions and can distort the junction potential such that the current spike causes more damage.

Very high-energy iron ions within the cosmic spectrum are of greatest concern for microelectronic circuitry in space. Generation of such ions is difficult and expansive in earth-based testing. Cyclotron damage simulation frequently uses energetic argon

---

[1]) Los Angeles, CA 90024, USA.

[2]) Research supported by the State of California through the MICRO Project, Grant No. UC-86-101, and the matching funds by TRW Corporation, Grant No. TRW-AN2700AL6S1, with UCLA.

63

and krypton ions having linear energy transfer characteristics similar to cosmic iron. Modeling and comparison of charge generation profiles for these ions is important for damage analyses and interpretation.

Previous efforts in modeling charge collection after production of these tracks have used assumptions for track width and density which have not been definitively established. Grubin et al. [1] assume an initial cylindrical track of radius 0.1 μm, an excess charge density of 10^{17} to 10^{19} per cm^3 constant across the track width, and a time of one ps for track production. A radially symmetric expression given by Jaffe [2] is used in an analysis by Messenger [3]

$$\delta_p = \frac{N}{\pi b^2} \exp\left(-\frac{r^2}{b^2}\right). \tag{1}$$

Here, δ_p is the volumetric electron–hole (e–h) pair generation along the ion path, b is the assumed track radius at $t=0$, and N is typically 10^7 to 10^{11} e–h pairs/cm. It was concluded that field motion typically starts after the ion track has expanded from an initial radius of 0.1 μm to about 1 μm, and that the track is created in about 500 ps.

Since the above models are derived from phenomenological and analytical approaches using unverified assumptions, a Monte Carlo-based analysis of electron generation and transport along ion tracks is useful in testing these assumptions. For this purpose, the ion transport code TRIPOS [4, 5] was extended to simulate secondary-electron generation and transport, with the transport mechanisms derived from the work of Fitting and Reinhardt [6].

2. Background

TRIPOS was developed by Chou and Ghoniem [4, 5] to study ion transport in solids using the Monte Carlo technique for the solution of the transport equation. TRIPOS is distinguished from other ion transport codes by its use of the power-law approximation to the Thomas-Fermi potential in the region between high ion energy (pure Coulombic interaction) and low ion energy (represented by a Born-Mayer interaction potential). TRIPOS also uses a number of variance reduction techniques and encompasses a variety of applications.

The slowing down of ions within the target material consists of two components: interaction with the target electrons and interaction with the nuclei. Electronic stopping is the dominant mechanism. At high ion velocities $v > v_0 Z_1^{2/3}$ (where $v_0 \approx c/137$ with c the speed of light) the electronic stopping power can be represented by the Bethe-Bloch formula

$$[S_e(E)]_{BB} = \frac{\Delta E}{\Delta x} = \frac{\pi Z_1^2 Z_2 e^4 N}{E} \log\left[\frac{T_{max}}{T_{min}}\right]. \tag{2}$$

Z_1 and Z_2 are the atomic numbers of the incident and target atoms respectively, e is the electronic charge, N is the target atom density, E is the incident ion energy, T_{min} corresponds to the mean ionization energy of the target atoms, and T_{max} represents the maximum kinetic energy transferable to a target particle

$$T_{max} = \frac{4 m_1 m_2}{(m_1 + m_2)^2} E. \tag{3}$$

In the Bethe-Bloch regime, the cross section for electronic energy transfer is represented by the Rutherford cross section

$$d\sigma = \pi \left[\frac{b}{2}\right]^2 T_{max} \frac{dT}{T^2}, \tag{4}$$

where b is the impact parameter and T represents the kinetic energy transferred to the target particle. The probability of energy transfer is inversely proportional to the square of the amount of kinetic energy transferred to the secondary electron (Fig. 1). The Bethe-Bloch equation for electronic stopping can be modified to give

$$S_e = C \log\left[\frac{T_{max}}{T_{cut}}\right] + C \log\left[\frac{T_{cut}}{T_{min}}\right], \tag{5}$$

where C is the collection of constants in (2). TRIPOS calculates S_e for each ion path. By choosing an arbitrary cutoff energy T_{cut}, energy transfers of magnitude greater than T_{cut} can be viewed as discrete energy transfers to high-energy secondary electrons. These electrons represent non-localized energy transfers because they can travel a significant distance away from the ion path before their kinetic energy is dissipated. By modeling transport of these high-energy secondaries, a computational model relevant to charged particle tracks in semiconductors can be developed and compared with the assumptions used in previous analyses. An analogous electronic stopping can also be calculated which represents all energy transfers to electrons of magnitude less than T_{cut}. This component represents a continuous energy transfer, localized to e–h pairs close to the ion path.

The Monte Carlo approach is used for both generation and transport of these high-energy secondary electrons. The probability distribution function f_p for kinetic energy transfer to electrons is given by (4) and Fig. 1. Integration between T_{max} and T_{cut} gives the cumulative distribution function f_c

$$f_c = \left[\frac{T_{max}T_{cut}}{T_{max} - T_{cut}}\right]\left[\frac{1}{T_{cut}} - \frac{1}{T}\right], \tag{6}$$

where T is the kinetic energy transferred to the electron. By choosing a random number between zero and one and equating it with the f_c, the corresponding energy transfer is calculated directly. Another random number is generated to represent the position of secondary-electron generation along the ion path. The kinetic energy of the generated electron is compared to the magnitude of the discrete component of the electronic energy loss between the successive nuclear scatterings. If the discrete component is less than the electron's kinetic energy, this discrete component is not sufficient for secondary-electron generation and this electron is discarded. If sufficient discrete energy exists for generation of additional electrons, they are created based on the conservation of discrete energy transfer.

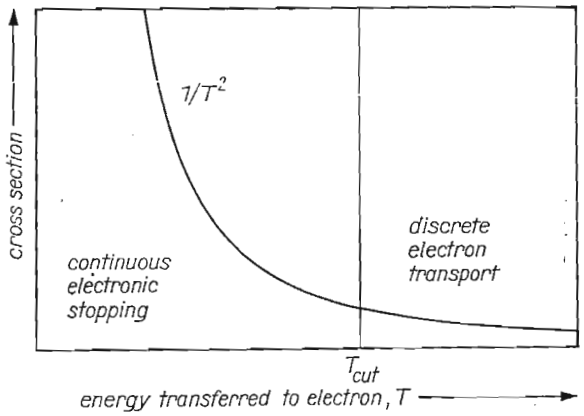

Fig. 1. Relative cross section for energy transfer

3. Electron Transport

The previously mentioned Bethe-Bloch theory accurately accounts for the transport of electrons with kinetic energies above 10 keV. At lower energies, better results are obtained by modeling electron transport using individual interaction mechanisms rather than a continuous energy-loss process.

Electron transport interaction mechanisms are divided into elastic and inelastic collisions. Elastic collisions involve scattering of the electron by nuclei with no change in kinetic energy. Inelastic interactions reduce the electron's energy, and consist of either ionization of core electrons or dielectric interaction with the valence electrons. The dielectric energy loss can be further divided into individual or collective electron–electron interactions (i.e. generation of either e–h pairs or plasmons). This is schematically shown in Fig. 2.

3.1 Elastic scattering

Two standard approaches are applied to the elastic scattering of electrons: Rutherford scattering and the partial waves method (PWM). For electrons with energies of 10 keV and above, elastic scattering can be modeled using the screened Rutherford interaction potential given by [6]

$$V(r) = -\frac{Ze}{4\pi\varepsilon_0}\frac{1}{r}\exp\left[-\frac{r}{r_s}\right], \tag{7}$$

with Z the atomic number of the target nucleus and r_s a screening radius. This potential incorporates a screening parameter representative of the screening of the nuclear charge by the surrounding bound electrons. The elastic scattering cross section is

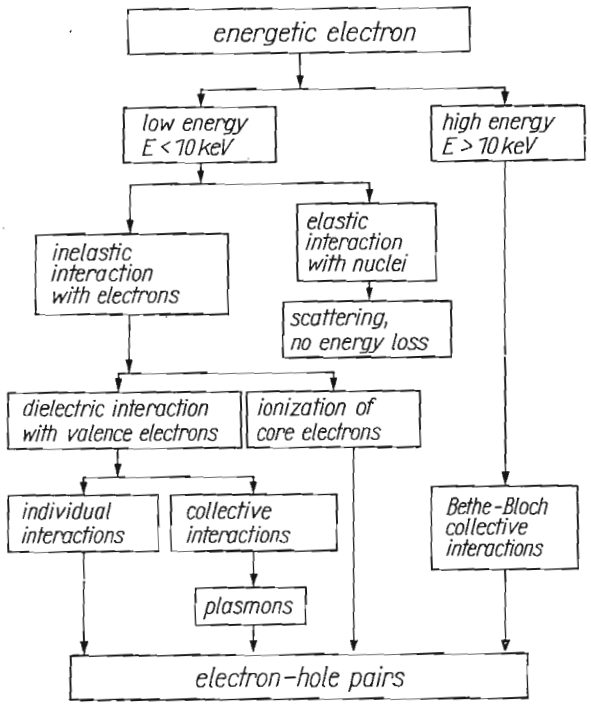

Fig. 2. Flowchart of electron slowing-down mechanisms

given by

$$\sigma_{el}(E) = \frac{2\pi Z^2 e^4}{(4\pi\varepsilon_0)^2} \frac{1}{4E^2} \frac{1}{2a_s(1+a_s)}, \tag{8}$$

with E the incident energy and the screening parameter a_s given by

$$a_s = \frac{\hbar^2}{8m_e E} \frac{1}{r_s^2}. \tag{9}$$

Different expressions for the screening parameter a_s are available (e.g. Nigam et al. [7]). Although calculations are straightforward, these equations give increasing error as electron energies decrease below 10 keV.

The PWM employs a quantum mechanical approximation for elastic scattering [8, 9]. The concept of wave-particle duality allows the incident particles to be considered as waves, and the scattering center acts as a perturbation. The magnitude of initial propagation constant k is the same, but the wave has a different direction and a different phase shift δ_l after scattering. The problem becomes that of determining the first several phase shifts using Schrödinger's equation with appropriate boundary conditions and interatomic potentials.

Several PWM analyses have been employed in modeling electron transport in a variety of materials (e.g. [10]). Fitting and Reinhardt [6] performed PWM analyses for several materials including silicon, but then compared the results to those of Rutherford scattering using the screening parameter

$$\tau(E) \approx 0.9 + \exp\left(-\frac{E}{E_\tau}\right), \tag{10}$$

which is related to the screening radius r_s of (7) and (9) by:

$$r_s = \frac{a_B}{Z^{1/3}}\left[\frac{0.885}{\tau} - \right], \tag{11}$$

where a_B is the Bohr radius. By choosing appropriate values of E_τ, good agreement was obtained between the two methods of calculation. Because of their simplicity, the formulas of Fitting et al. for elastic scattering cross sections were employed in this work to reduce computational effort.

3.2 Core electron ionization

Ionization of core electrons within a material is a significant energy loss mechanism for an energetic electron. A semiclassical approach for core ionization cross sections given by Gryzinski [11] was used by Akkerman et al. [10] and others. Fitting et al. [6] note that the core ionization stopping power can be represented in a form similar to the Bethe-Bloch equation, and the effective mean-free path for core ionization is then given by

$$\lambda_c = -\frac{\Delta E_c}{dE/dx}. \tag{12}$$

By ignoring any kinetic energy transfer to the ionized core electrons, ΔE_c is approximately equal to the mean core-ionization energy, I_c. Equation (12) can then be converted to the form:

$$\lambda_c = \frac{I_c E}{A \ln(E/I_c)}. \tag{13}$$

For silicon, Fitting et al. give values of 100 eV for I_c and 3000 eV^2/nm for the constant A, allowing direct calculation of the mean-free path for core ionization.

The polar scattering angle is approximated by a free collision momentum transfer

$$\sin^2\alpha \approx \frac{I_c}{E}. \tag{14}$$

3.3 Dielectric energy losses

An energetic electron can transfer energy to valence-band electrons by either plasmon production or creation of e–h pairs. Some previous modeling of electron transport uses detailed analytical expressions for dielectric energy loss by both mechanisms (e.g. [10]). As in [6], this work uses a simple scheme based on an empirical expression for inelastic mean-free path and on the previously defined core ionization mean-free path to calculate the mean-free path for dielectric interaction, λ_d. The equality

$$\lambda_{in}^{-1} = \lambda_c^{-1} + \lambda_d^{-1} \tag{15}$$

gives the value for λ_d once λ_{in} and λ_c are known.

Ashley and Tung [12] obtained equations for inelastic mean-free paths in silicon by analyzing experimental data. Rather than using the material-independent equation for λ_{in} given in [6], the equations in [12] are used in this work.

4. Monte Carlo Scheme

The Monte Carlo technique is based on a random determination of interaction parameters as defined by the governing equations. A sufficiently large collection of simulated particles should give a statistically valid average which is representative of actual behavior.

This work employs a random number determination for both path length and interaction mechanism. The path length is given by [10]

$$\lambda = -\lambda_{tot}\ln(\xi) = -(\sum \lambda_i^{-1})^{-1}\ln(\xi), \tag{16}$$

with ξ some random number between 0 and 1. The type of interaction i is determined from

$$P_{i-1} \leqq \xi \leqq P_i, \tag{17}$$

where $P_0 = 0$, $P_1 = \lambda_{tot}/\lambda_{el}$, $P_2 = \lambda_{tot}(\lambda_{el}^{-1} + \lambda_d^{-1})$, and $P_3 = \lambda_{tot}(\lambda_{el}^{-1} + \lambda_d^{-1} + \lambda_c^{-1}) = 1$.

For each elastic or dielectric interaction, the polar scattering angle α_i and any energy lost by the electron must be determined. The elastic scattering angle is determined by a random number, ξ_{el} [6]

$$\alpha_{el} = \cos^{-1}\left[1 - \frac{2a_s\xi_{el}}{1 + a_s - \xi_{el}}\right]. \tag{18}$$

Core ionizations involve an energy loss of 100 eV and an angle of scattering given by (14). Dielectric energy loss and scattering angle determinations require evaluation of the dielectric loss function, which for silicon is given in [6]. This loss function is evaluated from the complex dielectric constant of the material, which gives the experimental response of a system of atoms to an electromagnetic wave or in this case to the Coulombic force of a passing electron. A random number gives the dielectric energy loss ΔE

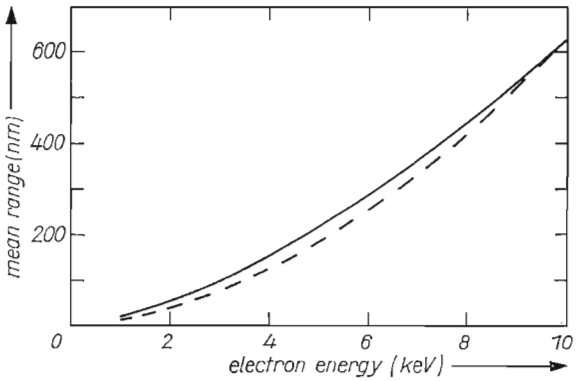

Fig. 3. Comparison of inelastic mean-free path formulas (——— from [13], – – – this work)

by application of the following equation:

$$\xi_d = \frac{\int_0^{\Delta E} \mathrm{Im}\,(-1/\varepsilon)\,\mathrm{d}E}{\int_0^{100\mathrm{eV}} \mathrm{Im}\,(-1/\varepsilon)\,\mathrm{d}E}, \tag{19}$$

where the denominator represents the area under the curve of the dielectric energy loss function. This integrated area is evaluated as a function of ΔE, and a fit of this data allows use of the random number scheme. After ΔE is evaluated, another random number can be directly related to the dielectric scattering angle α_d by an approach given in [6].

For each scattering event, the azimuthal scattering angle is also determined randomly between 0 and 2π.

To test the validity of the electron transport scheme used in TRIPOS-E, the code was used to model electron penetration at a surface with normal angle of incidence, and the mean range of all non-backscattered electrons was compared to an empirical formula for mean projected range of electrons in silicon as a function of energy given by [13]

$$R = 18E^{1.54}, \tag{20}$$

with R given in nm and E in keV. Fig. 3 shows good agreement between TRIPOS-E and (20), giving confidence in the approach used.

Different energy minima at which tracking of the electron was halted were compared. A minimum of 200 eV gives satisfactory agreement with (20), so this minimum energy value is used. This choice also adheres to the lower limit of validity for λ_{in} used in [12].

An additional routine is included for secondary electrons with energies above 10 keV, similar to the Bethe-Bloch formulation for ions represented by (2). A continuous energy-loss mechanism to the bulk electrons between elastic scatterings is assumed. The elastic scattering cross section is again given by (8), but now the screening parameter τ of (10) is set equal to 1. The Bethe-Bloch energy-loss equation is the same as that used by Shimizu et al. [14].

5. Secondary Electron Distributions

Four different incident high-energy ions of current interest are studied: 100 MeV proton, 180 MeV argon, 270 MeV krypton, and 1 GeV iron. Fig. 4 a and b shows 2D profiles of typical tracks for proton and krypton ions, respectively, where the end-

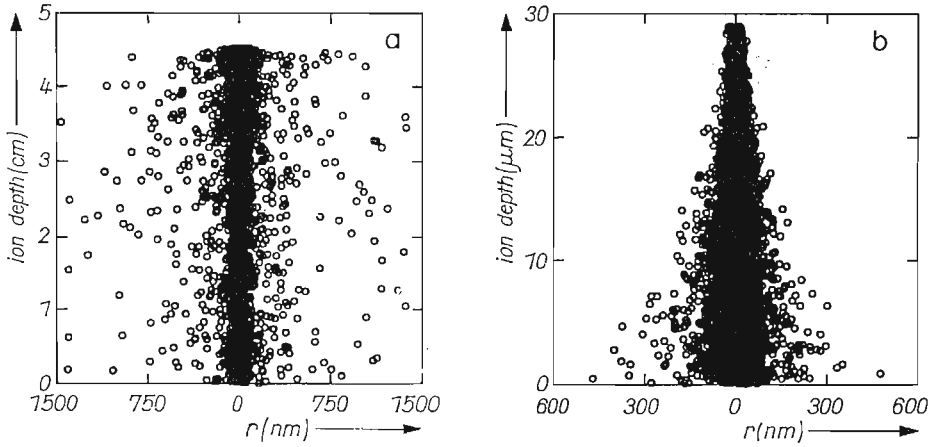

Fig. 4. Two-dimensional profile of secondary electron ranges in silicon as a function of track depth for: a) 100 MeV proton, b) 270 MeV krypton

point of each generated secondary electron (i.e. the point where the kinetic energy falls below 200 eV) is plotted with respect to the ion path. Changes in the direction of the ion path because of collisions are not shown; a straight line path is simulated.

The minimum energy of generated secondary electrons is assumed to be 1 keV. As the ion loses energy it reaches a point toward the end of its track where it can no longer generate 1 keV secondaries, in agreement with (3). This behavior is particularly evident for heavier ions, as in Fig. 4 b.

The secondaries arising from protons and other light ions have a higher average energy at creation than those from heavy ions, and tend to travel further. This fact is representative of better energy coupling between the electrons and the light ion, as expected from (3). The initial energy of the secondaries at creation decreases as an ion loses energy, resulting in a shorter range for the electrons generated further along the track. This behavior is most notable for heavy ions, resulting in the funnel-shaped tracks apparent in Fig. 4 b.

An evaluation was made of the average time spent by the electrons between generation and reduction of energy below 200 eV. For all ions, the average time is in the order of 10^{-14} s, indicating very rapid track generation.

6. Electron-Hole Pair Distribution

Each secondary electron undergoes many inelastic collisions between generation and thermalization. To evaluate this energy deposition radially from the track, a series of concentric zones are set up around the track and energy losses within each zone are tabulated. These losses are considered to be deposited locally, and the radial e–h pair densities can be obtained by dividing the total energy deposition within each zone by the energy required to produce an e–h pair (i.e. 3.6 eV in silicon). Results for the radial distributions of e–h pairs can be fit to an equation to express the distribution in a convenient form. As some track widths change with depth into the medium, several positions along the track are evaluated in terms of the energy deposition within a slice of the silicon material (e.g. a 1 μm-thick slice perpendicular to the direction of ion penetration).

Results of this analysis are shown in Fig. 5 a and b for 270 MeV krypton and 1 GeV iron ions. These figures indicate an exponential tail for the charge distribution away

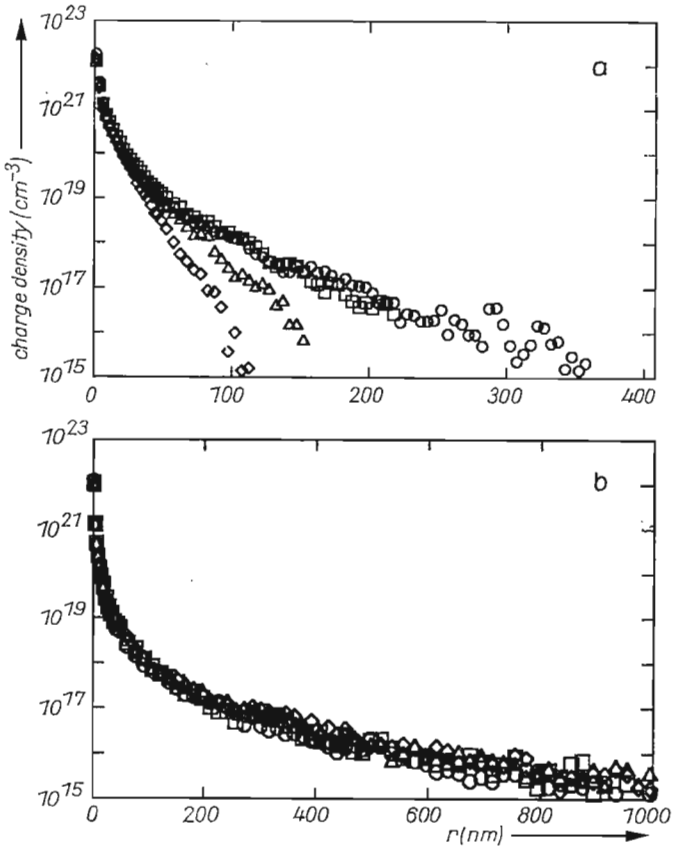

Fig. 5. Radial volumetric charge density in silicon due to high-energy secondary electrons using $T_{cut} = 1000$ eV for: a) 270 MeV krypton (depth: ○ 5, □ 10, △ 15, ◇ 20 μm), b) 1 GeV iron (depht: ○ 5, △ 10 μm)

from the central core of the ion path, suggestive of penetration by the high-energy secondary electrons. A cutoff energy of 1 keV for secondary generation is used for these figures. The narrowing of the charge-density profiles in Fig. 5a for the krypton ion at increasing depth reflects the reduced probability of generation of high-energy secondaries as the ion loses energy.

Fig. 5 a and b reflect charge generation arising only from the secondary electrons. The low-energy transfer to electrons below the cutoff energy must also be accounted for in a total charge-density profile. For this low-energy deposition, a Gaussian profile can be postulated similar to that of (1) which can also account for the non-exponential behavior of Fig. 5 a and b at small values of radial distance. Combining the Gaussian and exponential components in an expression for charge-density profile gives

$$\eta(r) = C\frac{1}{r}\left[\exp\left(-\frac{r^2}{b_1^2}\right) + \xi\exp\left(-\frac{r}{b_2}\right)\right], \tag{21}$$

where C is some constant, b_1 and b_2 are analogous to track widths for the Gaussian and exponential regions, respectively (as in (1)), ξ is a correlation factor between the two components, and the $1/r$ dependency reflects the cylindrical geometry. Equation (21) can be integrated over r from zero to infinity to obtain the total charge deposition.

which in turn provides an expression for the constant C and gives

$$r\eta(r) = \frac{N_t}{\pi^{3/2}b_1 + 2\pi\xi b_2}\left[\exp\left(-\frac{r^2}{b_1^2}\right) + \xi\exp\left(-\frac{r}{b_2}\right)\right], \tag{22}$$

where N_t is the total charge deposition along a unit path length of the ion. Fig. 6a is a conversion of Fig. 5a (5 μm depth) to a graph of $\ln[r\eta(r)]$ versus r, in which the exponential tail is still apparent. Note that the exponential portion of (22) can be expressed in the form

$$\ln[r\eta(r)] = \ln\frac{N_t\xi}{\pi^{3/2}b_1 + 2\pi\xi b_2} - \frac{r}{b_2}. \tag{23}$$

The slope along the linear portion of Fig. 6a provides a value for b_2, and extrapolation of the linear portion to $r = 0$ and comparison with (23) gives an expression for $\xi = \xi(b_1)$. The Gaussian component reflected by b_1 accounts for both the curved region of Fig. 6a at small values of r and an additional enhancement within that region due to the low energy transfers. Equation (22) can be converted into a form dependent only on r and b_1, which should give good agreement throughout the linear portion of

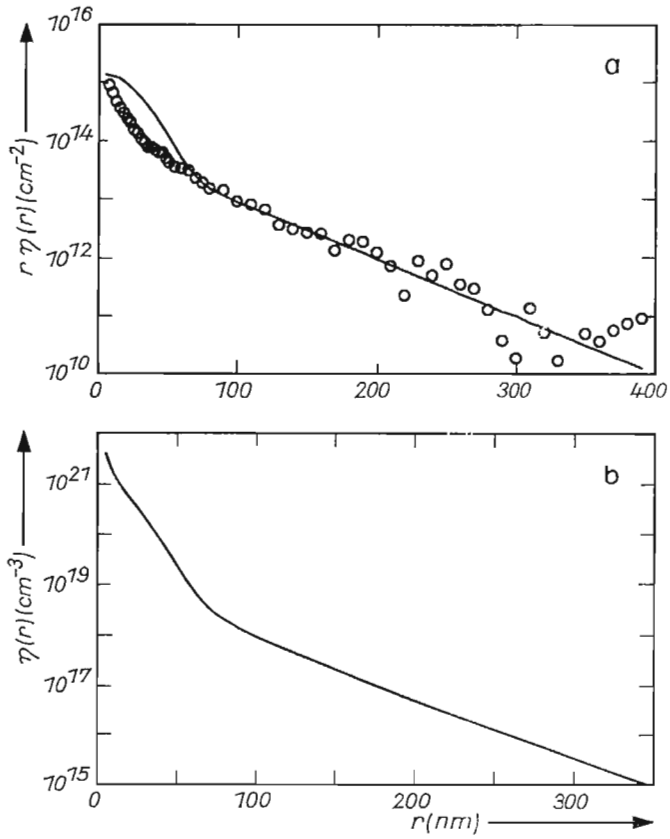

Fig. 6. 270 MeV krypton incident on silicon, at 5 μm depth, using $T_{cut} = 1000$ eV: a) comparison of the analytical formula to the computational results from TRIPOS-E for radial charge surface density (○ Monte Carlo, fast electrons, ——— analytical, all electrons), b) radial volumetric density profile, given by the analytical formula

Table 1
Parameters for analytical track profiles

T_c (eV)	5 μm depth			10 μm depth		
	b_1 (nm)	b_2 (nm)	ξ	b_1 (nm)	b_2 (nm)	ξ
270 MeV krypton						
500	26.5	63.9	0.0695	22.5	43.7	0.0874
1000	29.5	44.6	0.0622	22.5	27.6	0.104
1500	19.0	31.4	0.135	17.5	24.8	0.158
180 MeV argon						
200	38.0	103.7	0.0879	31.0	87.2	0.0822
500	30.5	91.9	0.0732	43.0	95.6	0.0671
1000	35.5	85.0	0.0606	36.5	77.7	0.0643
2000	29.0	50.9	0.123	28.0	61.2	0.109

Fig. 6a. Thus, a least-squares comparison of this equation to the data throughout the linear regime can provide the "best" value of b_1. With b_1 determined, a value for the parameter ξ is obtained directly from the expression $\xi = \xi(b_1)$.

The results from one of these analyses are also shown in Fig. 6a, where the analytical expression with evaluated values of b_1, b_2, and ξ are compared with the output of TRIPOS-E. Good agreement is apparent throughout the exponential regime, and the higher density core contains all low-energy transfers. This data is replotted in Fig. 6b as $\eta(r)$ versus r, to show the relative magnitude of the charge core more clearly.

To evaluate the effect of the choice of cutoff energy on the values of these parameters, several analyses are performed using cutoff energies ranging from 200 eV to 2 keV. Results for b_1 and b_2 for 270 MeV krypton and 180 MeV argon are listed in Table 1. For krypton, b_2 extrapolates to about 80 nm for a depth in silicon of 5 μm and drops off rapidly as the depth of penetration increases. For argon, b_2 extrapolates to approximately 100 nm. Both ions give similar values for b_1: approximately 30 nm for krypton and 40 nm for argon. Values for ξ range between 0.06 and 0.16 for both ions. These values for b_1 and b_2 approach a plateau at lower values of cutoff energy. Low values of T_{cut} should give more accurate results, but with greater computing costs. The above results indicate a choice of T_{cut} in the range of 0.5 to 1.0 keV should give satisfactory accuracy.

7. Significance of Results

The radial distance over which the excess charge carrier concentrations remain above background dopant levels (typically 10^{16} cm^{-3}) is important for analysis of transient behavior. Fig. 5a shows this distance to exceed 0.25 μm for 270 MeV krypton. The corresponding value for 180 MeV argon was found to be greater than 0.33 μm. Fig. 5b shows this distance to exceed 0.5 μm for 1 GeV iron. These values are greater than the previously mentioned assumptions for track width in [1] and [3]. The larger track widths and faster generation times indicated by TRIPOS-E are important for modeling the transient current spikes arising from ion passage. Results from TRIPOS-E indicate an exponential charge generation profile extending hundreds of nanometers from the ion path; such a profile has never been postulated in previous models of track structure.

Different results for the radial extent of the tracks of cosmic iron and those arising from cyclotron simulations also raise issues relating to the accuracy of cyclotron simulation of cosmic damage of microelectronic circuitry. The axial charge-generation profile apparent in Fig. 5a for krypton will not be apparent over microelectronic device dimensions for ions of such high energy as cosmic iron, possibly affecting quantitative analyses using cyclotron simulation.

Parameters have been evaluated to provide analytical expressions for the charge-density profiles along heavy ion paths. These expressions provide much more detail than previous assumptions for radial charge profiles, and should prove useful and convenient in future modeling of charge transport along ion tracks in semiconductor devices.

Acknowledgements

This work was supported by the State of California through the MICRO Project, Grant No. UC-86-101, and the matching funds by TRW Corporation, Grant No. TRW-AN2700AL6S, with UCLA.

References

[1] H. L. Grubin, J. P. Kreskovsky, and B. C. Weinberg, IEEE Trans. Nuclear Sci **31**, 1161 (1984).
[2] G. Jaffe, Ann. Phys. **42**, 303 (1913).
[3] G. C. Messenger, IEEE Trans. Nuclear Sci. **29**, 2024 (1982).
[4] P. Chou and N. M. Ghoniem, J. Nuclear Mater. (Amsterdam) **117**, 55 (1983).
[5] P. S. Chou and N. M. Ghoniem, Nuclear Instrum. and Methods Phys. Res. B **28**, 175 (1987).
[6] H.-J. Fitting and J. Reinhardt, phys. stat. sol. (a) 88, 245 (1985).
[7] B. P. Nigam, M. K. Sundaresan, and Ta-You Wu, Phys. Rev. **115**, 491 (1959).
[8] R. C. Martin and N. M. Ghoniem, Coupled Ion-Electron Transport in Semiconductors, University of California, Los Angeles Report No. UCLA-ENG-87-8/PPG-1024, 1987.
[9] E. E. Anderson, Modern Physics and Quantum Mechanics, Chap. 11, W. B. Saunders Publ. Co., Philadelphia 1971.
[10] A. F. Akkerman and A. L. Gibrekhterman, Nuclear Instrum. and Methods Phys. Res. **B6**, 496 (1985).
[11] M. Gryzinski, Phys. Rev. **138**, 336 (1965).
[12] J. C. Ashley and C. J. Tung, Surface Interface Anal. **4**, 52 (1982).
[13] A. Ya. Vyatskin and V. V. Trunev, Radiotekhnika i Elektronika **12**, 1636 (1967).
[14] R. Shimuzu, T. Ikuta, and K. Murata, J. appl. Phys. **43**, 4233 (1972).

(Received July 24, 1987)